

Instabilities of soft elastic microtubes filled with viscous fluids: Pearls, wrinkles, and sausage stringsGaurav Tomar,^{1,*} Dipankar Bandopadhyay,^{2,†} and Ashutosh Sharma^{3,4,‡}¹*Department of Mechanical Engineering, Indian Institute of Science, Bangalore, India*²*Department of Chemical Engineering, Indian Institute of Technology, Guwahati, India*³*Department of Chemical Engineering, Indian Institute of Technology, Kanpur, India*⁴*School of Mechanical Engineering, Yeungnam University, Gyongsan, South Korea*

(Received 21 June 2011; revised manuscript received 15 August 2011; published 16 September 2011)

A linear stability analysis is presented to study the self-organized instabilities of a highly compliant elastic cylindrical shell filled with a viscous liquid and submerged in another viscous medium. The prototype closely mimics many components of micro- or nanofluidic devices and biological processes such as the budding of a string of pearls inside cells and sausage-string formation of blood vessels. The cylindrical shell is considered to be a soft linear elastic solid with small storage modulus. When the destabilizing capillary force derived from the cross-sectional curvature overcomes the stabilizing elastic and in-plane capillary forces, the microtube can spontaneously self-organize into one of several possible configurations; namely, pearling, in which the viscous fluid in the core of the elastic shell breaks up into droplets; sausage strings, in which the outer interface of the microtube deforms more than the inner interface; and wrinkles, in which both interfaces of the thin-walled microtube deform in phase with small amplitudes. This study identifies the conditions for the existence of these modes and demonstrates that the ratios of the interfacial tensions at the interfaces, the viscosities, and the thickness of the microtube play crucial roles in the mode selection and the relative amplitudes of deformations at the two interfaces. The analysis also shows asymptotically that an elastic fiber submerged in a viscous liquid is unstable for $Y = \gamma/(G_e R) > 6$ and an elastic microchannel filled with a viscous liquid should rupture to form spherical cavities (pearling) for $Y > 2$, where γ , G_e , and R are the surface tension, elastic shear modulus, and radius, respectively, of the fiber or microchannel.

DOI: [10.1103/PhysRevE.84.031603](https://doi.org/10.1103/PhysRevE.84.031603)

PACS number(s): 68.03.-g, 47.55.nb, 47.61.-k, 46.35.+z

I. INTRODUCTION

Recent advances in the miniaturization of the technological devices have offered a renewed interest in studying the self-organized deformations of compliant tubes, sheets, and fibers of micro- or nanodimensions. Self-organizing flexible tubular or sheet-like structures are very common in micro-electromechanical systems (MEMS) [1,2], drug delivery modules [3–5], cell cytoskeletons [6], and sensor applications [7,8]. Deforming “soft” microfibers or microtubes also mimics some biological phenomena; for example, budding of a string of pearls during the cell locomotion and in Golgi bodies [9,10], fusion and fission of cell membranes [11], instabilities in the axons and dendrons [12–17], and sausage-string patterns in blood vessels during high blood pressure [18], among others. Interestingly, instabilities of fibrous structures such as in electrospun micro- or nanofibers [19,20] and in the buckling of large-aspect-ratio fibrillar adhesives on gecko feet [21–25] also show Rayleigh instability characteristics. Thus, extensive research has been directed to the self-organized instabilities of microfibers and microtubes, especially when they are composed of compliant smart materials such as soft polymers, gels, and biological tissues.

Previous studies show that polymer gels can undergo phase transitions and elastic instabilities in response to thermal or solutal variations [10,11]. Matsuo and Tanaka showed that the cylindrical gels can deform into bubbles and/or

bamboo patterns on a shrinking gel when the outer shell is denser [12,13]. These studies point to the fact that the instabilities in soft microfibers and microtubes are similar to the Rayleigh-Plateau instability [26,27] of a liquid discharging from a faucet at low flow rates and breaking into droplets. In such situations, the length scale of the instability is determined from the competing stabilizing capillary forces because of the curvature in the plane containing the axis of the cylinder and the destabilizing capillary force, which is a function of the local radius of the cylinder [26, 28]. The critical condition for the onset of this instability is $kR < 1$, where k is the wave number and R is the radius of the cylinder [26]. The wavelength and growth rate of the dominant mode can be determined by considering the rate-determining kinetic parameters such as viscosity [27,29].

In contrast to liquid threads, which are unconditionally unstable under the Rayleigh-Plateau instability, the elastic energy penalty against deformations tends to stabilize elastic tubes and fibers. Thus, a soft compliant tube can become unstable for a set of modes determined by the competition between the stabilizing elastic and destabilizing capillary forces when a critical magnitude of destabilization is present. Capillary instabilities in thin solid films have been analyzed by McCallum *et al.* [30] by including surface diffusion as the mode of mass transfer in contrast to fluids where viscous flow dominates. It was concluded that all the unstable perturbations are of the varicose type. Following a similar approach, Yang and Song analyzed the linear stability of elastic axisymmetrical surface coatings [31].

In the present study, we analyze the elastic instabilities of a linearly elastic tube filled with and surrounded by similar or dissimilar viscous liquids, as schematically shown in Fig. 1.

*gtom@mecheng.iisc.ernet.in

†dipban@iitg.ac.in

‡ashutos@iitk.ac.in

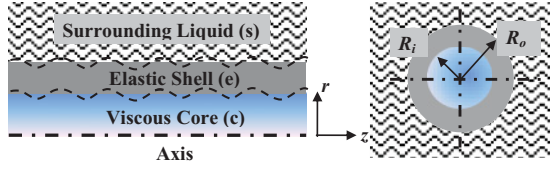


FIG. 1. (Color online) Schematic of axisymmetric and cross-sectional view of a hollow cylinder filled and surrounded by viscous liquids.

The theoretical framework employed here is similar to the stability analysis of thin soft elastic solid films [32–58] that are rendered unstable by an externally applied field, such as van der Waals [32–36,40–43,48,52,57,58] and electrostatic forces [49,53,57], and stabilized by the elastic strain energy and the in-plane curvature. This theoretical approach has shown agreement with experiments on thin soft cross-linked polydimethylsiloxane (PDMS) films [32,59–64]. In contrast to the previous thin film studies, destabilization is caused by the out-of-plane curvature in the microtubes being considered here, and the instability modes are also modified by the presence of viscous fluids in the core and outer surroundings of the tube. The linear stability analysis (LSA) of the governing equations shows different types of self-organized interfacial patterns: (i) pearling, in which the viscous fluid in the core breaks up into structures resembling a string of pearls or peapods [Fig. 2(a)]; (ii) sausage strings, in which the outer interface of the microtube deforms more than the inner interface [Fig. 2(b)]; and (iii) wrinkles, which consists of in-phase small-amplitude deformations of the microtube [Fig. 2(c)]. The LSA for an elastic annulus surrounded by viscous fluids also demonstrate the characteristics of a number of asymptotic cases; namely, the flow of a thin liquid microcapillary thread

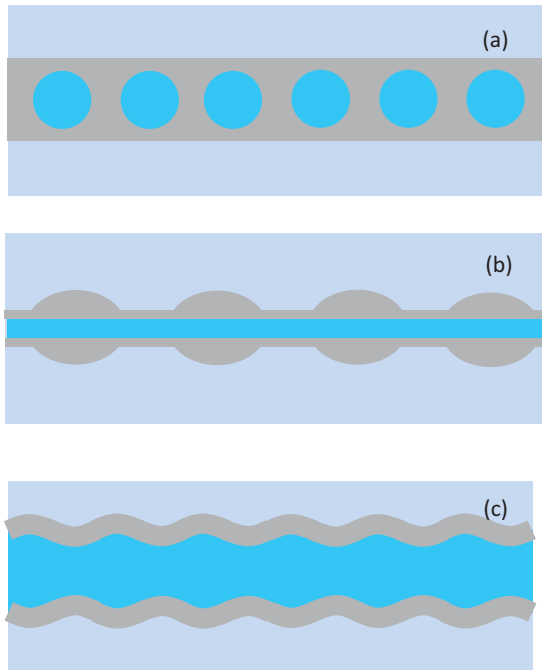


FIG. 2. (Color online) Schematic showing the possible modes of deformations of the inner and outer surfaces: (a) pearling, (b) sausage strings, and (c) wrinkling.

surrounded by an elastic medium and a thin elastic fiber submerged in a viscous fluid. The salient features of the instabilities of these asymptotic systems are also studied in detail.

II. PROBLEM FORMULATION

The schematic of the viscous core, elastic annulus, and the surrounding viscous medium under study is shown in Fig. 1. The inner and outer radii of the elastic annulus are represented by R_i and R_o , respectively. The broken lines depict possible deformations of amplitude ε_i and ε_o at the inner and outer surfaces, respectively. The viscosity of the liquid inside the core is μ_c and that of the surrounding liquid is μ_s . The elastic shear modulus of the homogeneous isotropic elastic annulus is G_e . The liquids and the elastic material are assumed to be incompressible. The inertial forces are neglected as the radius of the elastic tube is small and the surrounding medium is in a quiescent state. The following radial (r component) and the axial (z component) equations of motion and the continuity equations describe the motion of an axisymmetric elastic annulus with a viscous core and a surrounding viscous medium.

A. Governing equations

The following equations describe the dynamics of the viscous core and the viscous fluid surrounding the elastic cylindrical shell:

$$\mu_i \left[\frac{1}{r} \frac{\partial}{\partial r} \left(r \frac{\partial v_z^{(i)}}{\partial r} \right) + \frac{\partial^2 v_z^{(i)}}{\partial z^2} \right] - \frac{\partial P_i}{\partial z} = 0, \quad (1)$$

$$\mu_i \left[\frac{\partial}{\partial r} \left(\frac{1}{r} \frac{\partial (r v_r^{(i)})}{\partial r} \right) + \frac{\partial^2 v_r^{(i)}}{\partial z^2} \right] - \frac{\partial P_i}{\partial r} = 0, \quad (2)$$

$$\frac{1}{r} \frac{\partial (r v_r^{(i)})}{\partial r} + \frac{\partial v_z^{(i)}}{\partial z} = 0. \quad (3)$$

The equations of motion for the liquid are written in terms of velocity $\{v_r^{(i)}, v_z^{(i)}\}$ and pressure P_i , where i in the subscript or superscript is a placeholder for “c” and “s” denoting the viscous core and the surrounding viscous medium, respectively. Subscripts “r” and “z” denote the radial and axial direction components, respectively.

The following equations of motion and the condition for incompressibility describe the deformations in the elastic tube:

$$G_e \left[\frac{1}{r} \frac{\partial}{\partial r} \left(r \frac{\partial u_z^{(e)}}{\partial r} \right) + \frac{\partial^2 u_z^{(e)}}{\partial z^2} \right] - \frac{\partial P_e}{\partial z} = 0, \quad (4)$$

$$G_e \left[\frac{\partial}{\partial r} \left(\frac{1}{r} \frac{\partial (r u_r^{(e)})}{\partial r} \right) + \frac{\partial^2 u_r^{(e)}}{\partial z^2} \right] - \frac{\partial P_e}{\partial r} = 0, \quad (5)$$

$$\frac{1}{r} \frac{\partial (r u_r^{(e)})}{\partial r} + \frac{\partial u_z^{(e)}}{\partial z} = 0. \quad (6)$$

In the absence of the body forces and inertia, the stress field $\boldsymbol{\sigma}$ of an incompressible linear elastic material satisfies $\nabla \cdot \boldsymbol{\sigma} = 0$ [yielding Eqs. (4) and (5)], where $\boldsymbol{\sigma} = -P_e \mathbf{I} + G_e (\nabla \mathbf{u}^{(e)} + \nabla \mathbf{u}^{(e)T})$ and $\mathbf{u} = \{u_r^{(e)}, u_z^{(e)}\}$ is the displacement field. Here, the superscripts and subscripts “e” denote quantities for the elastic medium. The momentum balance equations are supplemented by an explicit incompressibility condition given by Eq. (6).

Since the elastic deformations are instantaneous (or have a fast time scale), the time scale of instability in this system is governed by the viscous nature of the two fluids that surround the tube wall.

B. Boundary conditions

We assume that the flow is axisymmetric and there is no radial flow at $r = 0$:

$$v_r^{(c)} = 0, \quad (7)$$

$$\frac{\partial v_z^{(c)}}{\partial r} = 0. \quad (8)$$

At $r = R_i$, continuity of velocity components, the normal stress balance, shear stress balance, and the kinematic condition are given by

$$v_r^{(c)} = \frac{\partial u_r^{(e)}}{\partial t} \text{ and } v_z^{(c)} = \frac{\partial u_z^{(e)}}{\partial t}, \quad (9)$$

$$P_c - P_e - 2\mu_c \frac{\partial v_r^{(c)}}{\partial r} + 2G_e \frac{\partial u_r^{(e)}}{\partial r} + \gamma_i \kappa_i = 0, \quad (10)$$

$$\mu_c \left(\frac{\partial v_z^{(c)}}{\partial r} + \frac{\partial v_r^{(c)}}{\partial z} \right) = G_e \left(\frac{\partial u_z^{(e)}}{\partial r} + \frac{\partial u_r^{(e)}}{\partial z} \right), \quad (11)$$

$$\frac{\partial R_i}{\partial t} + v_z^{(c)} \Big|_{R_i} \frac{\partial R_i}{\partial z} = v_r^{(c)} \Big|_{R_i}. \quad (12)$$

Here, $a|_{R_i}$ implies any variable a evaluated at the inner radius R_i of the elastic tube, κ_i is the curvature at the inner surface, and γ_i is the surface tension coefficient at the inner surface of the tube.

At the outer radius of the elastic tube, $r = R_o$, continuity of the velocity components, the normal stress, the shear stress balance, and the kinematic condition are given respectively by

$$v_r^{(s)} = \frac{\partial u_r^{(e)}}{\partial t} \text{ and } v_z^{(s)} = \frac{\partial u_z^{(e)}}{\partial t}, \quad (13)$$

$$P_e - P_s + 2\mu_s \frac{\partial v_r^{(s)}}{\partial r} - 2G_e \frac{\partial u_r^{(e)}}{\partial r} + \gamma_o \kappa_o = 0, \quad (14)$$

$$\mu_s \left(\frac{\partial v_z^{(s)}}{\partial r} + \frac{\partial v_r^{(s)}}{\partial z} \right) = G_e \left(\frac{\partial u_z^{(e)}}{\partial r} + \frac{\partial u_r^{(e)}}{\partial z} \right), \quad (15)$$

$$\frac{\partial R_o}{\partial t} + v_z^{(s)} \Big|_{R_o} \frac{\partial R_o}{\partial z} = v_r^{(s)} \Big|_{R_o}, \quad (16)$$

where γ_o is the surface tension coefficient at the outer surface of the tube and κ_o is the curvature at the outer surface of the elastic tube. Curvatures at the inner and outer radius in the small-slope approximation are given by $\kappa_i \approx R_{i,zz} + 1/R_i$ and $\kappa_o \approx R_{o,zz} + 1/R_o$, respectively, where the subscript ‘‘zz’’ represents the second derivative with respect to the axial direction z .

III. LINEAR STABILITY ANALYSIS

The dimensional form of Eqs. (1)–(16) can be nondimensionalized as follows: The radial r and axial z coordinates and displacements in the elastic annulus are nondimensionalized by the inner radius of the elastic annulus, R_i . The velocity field and the pressure and stress are nondimensionalized by $\gamma_i/(\mu_c R_i)$ and γ_i/R_i , respectively, and time is nondimensionalized by the parameter $\gamma_i/(\mu_c R_i^2)$. In what follows, all quan-

ties (time, velocities, displacements, and pressure) are in the nondimensional form, including the coordinates r and z . In order to perform LSA, the nondimensionalized form of the governing equations [Eqs. (1)–(6)] are linearized using the following nondimensional axisymmetric normal linear modes: $v_z^{(c)} = \tilde{v}_z^{(c)} e^{\Omega t + i K z}$, $v_r^{(c)} = \tilde{v}_r^{(c)} e^{\Omega t + i K z}$, $u_z^{(e)} = \tilde{u}_z^{(e)} e^{\Omega t + i K z}$, $u_r^{(e)} = \tilde{u}_r^{(e)} e^{\Omega t + i K z}$, $v_z^{(s)} = \tilde{v}_z^{(s)} e^{\Omega t + i K z}$, $v_r^{(s)} = \tilde{v}_r^{(s)} e^{\Omega t + i K z}$, $P_j = \tilde{P}_j + \tilde{P}_j e^{\Omega t + i K z}$, where Ω and K are the nondimensional linear growth rate and wave number, respectively, subscript j stands for ‘‘c,’’ ‘‘e,’’ and ‘‘s’’ representing the parameters in the core, soft elastic solid, and the surrounding medium, respectively, and \tilde{P}_j is the base state pressure. The base state pressure is the capillary pressure in the undeformed cylinder due to the radius of the cylinder. The nondimensional linear growth rate (Ω) and the wave number (K) of the instability can be written in terms of the dimensional growth rate ω and wave number k as $\Omega = \omega \gamma_i / (\mu_c R_i^2)$ and $K = k R_i$, respectively. Perturbed radii $\tilde{R}_j = \bar{R}_j + \varepsilon_j e^{\Omega t + i K z} + O(\varepsilon_j^2)$ where $j = i$ and o represents the value of the local nondimensional radius at the inner ($\bar{R}_i = 1$) and the outer surface ($\bar{R}_o = 1/\beta$), respectively, of the elastic annulus. Here, \tilde{R}_j is the nondimensionalized perturbed radius and \bar{R}_j is the base state nondimensionalized radius. The parameter $\beta = R_i/R_o$ is the ratio of the inner and outer radii of the elastic annulus. A nondimensional parameter giving a measure of the stabilizing elastic forces in comparison to the destabilizing capillary pressure can be written as $Y = \gamma_i/(G_e R_i)$. The sinusoidal perturbations on an axisymmetric fiber correspond to a second-order change in the base state radius [$O(\varepsilon_j^2)$] for volume conservation, which we neglect in our first-order analysis. Using the above defined nondimensionalized linearized parameters the governing equations [Eqs. (1)–(6)] can be written as

$$-i K \tilde{P}_c + \left[\frac{1}{r} \frac{\partial}{\partial r} \left(r \frac{\partial \tilde{v}_z^{(c)}}{\partial r} \right) - K^2 \tilde{v}_z^{(c)} \right] = 0, \quad (17)$$

$$-\frac{\partial \tilde{P}_c}{\partial r} + \left[\frac{\partial}{\partial r} \left(\frac{1}{r} \frac{\partial (r \tilde{v}_r^{(c)})}{\partial r} \right) - K^2 \tilde{v}_r^{(c)} \right] = 0, \quad (18)$$

$$\tilde{v}_z^{(c)} = -\frac{1}{i K r} \frac{\partial (r \tilde{v}_r^{(c)})}{\partial r}, \quad (19)$$

$$-i K \tilde{P}_e + \frac{1}{Y} \left[\frac{1}{r} \frac{\partial}{\partial r} \left(r \frac{\partial \tilde{u}_z^{(e)}}{\partial r} \right) - K^2 \tilde{u}_z^{(e)} \right] = 0, \quad (20)$$

$$-\frac{\partial \tilde{P}_e}{\partial r} + \frac{1}{Y} \left[\frac{\partial}{\partial r} \left(\frac{1}{r} \frac{\partial (r \tilde{u}_r^{(e)})}{\partial r} \right) - K^2 \tilde{u}_r^{(e)} \right] = 0, \quad (21)$$

$$\tilde{u}_z^{(e)} = -\frac{1}{i K r} \frac{\partial (r \tilde{u}_r^{(e)})}{\partial r}, \quad (22)$$

$$-i K \tilde{P}_s + \frac{1-M}{M} \left[\frac{1}{r} \frac{\partial}{\partial r} \left(r \frac{\partial \tilde{v}_z^{(s)}}{\partial r} \right) - K^2 \tilde{v}_z^{(s)} \right] = 0, \quad (23)$$

$$-\frac{\partial \tilde{P}_s}{\partial r} + \frac{1-M}{M} \left[\frac{\partial}{\partial r} \left(\frac{1}{r} \frac{\partial (r \tilde{v}_r^{(s)})}{\partial r} \right) - K^2 \tilde{v}_r^{(s)} \right] = 0, \quad (24)$$

$$\tilde{v}_z^{(s)} = -\frac{1}{i K r} \frac{\partial (r \tilde{v}_r^{(s)})}{\partial r}. \quad (25)$$

where the variables $\tilde{v}_z^{(c)}$, $\tilde{v}_r^{(c)}$, $\tilde{u}_z^{(e)}$, $\tilde{u}_r^{(e)}$, $\tilde{v}_z^{(s)}$, $\tilde{v}_r^{(s)}$, \tilde{P}_j , and ε_j (subscript $j = i$ and o represents inner and outer surfaces of

the elastic annulus, respectively) are functions of the radial coordinate r only. The parameter M is a function of the ratio of the viscosities of the core and surrounding fluids and is given by $M = \mu_c/(\mu_c + \mu_s)$. Eliminating \tilde{P}_c , \tilde{P}_e , and \tilde{P}_s forms the linearized governing equations [Eqs. (17)–(25)] and we obtain the following biharmonic equations in $\tilde{v}_r^{(c)}$, $\tilde{u}_r^{(e)}$, and $\tilde{v}_r^{(s)}$:

$$\left\{ \frac{d}{dr} \frac{1}{r} \frac{d}{dr} \left[r \frac{d}{dr} \left(\frac{1}{r} \frac{d(rv_r^{(c)})}{dr} \right) \right] - 2K^2 \left(\frac{d}{dr} \frac{1}{r} \frac{d(rv_r^{(c)})}{dr} \right) + K^4 v_r^{(c)} \right\} = 0, \quad (26)$$

$$\left\{ \frac{d}{dr} \frac{1}{r} \frac{d}{dr} \left[r \frac{d}{dr} \left(\frac{1}{r} \frac{d(ru_r^{(e)})}{dr} \right) \right] - 2K^2 \left(\frac{d}{dr} \frac{1}{r} \frac{d(ru_r^{(e)})}{dr} \right) + K^4 u_r^{(e)} \right\} = 0, \quad (27)$$

$$\left\{ \frac{d}{dr} \frac{1}{r} \frac{d}{dr} \left[r \frac{d}{dr} \left(\frac{1}{r} \frac{d(rv_r^{(s)})}{dr} \right) \right] - 2K^2 \left(\frac{d}{dr} \frac{1}{r} \frac{d(rv_r^{(s)})}{dr} \right) + K^4 v_r^{(s)} \right\} = 0. \quad (28)$$

The general solutions of Eqs. (26)–(28) are the following:

$$\tilde{v}_r^{(c)}(r) = A_1 r K_0(Kr) + A_2 K_1(Kr) + A_3 r I_0(Kr) + A_4 I_1(Kr), \quad (29)$$

$$\tilde{u}_r^{(e)}(r) = B_1 r K_0(Kr) + B_2 K_1(Kr) + B_3 r I_0(Kr) + B_4 I_1(Kr), \quad (30)$$

$$\tilde{v}_r^{(s)}(r) = C_1 r K_0(Kr) + C_2 K_1(Kr) + C_3 r I_0(Kr) + C_4 I_1(Kr). \quad (31)$$

Here, the coefficients A_i , B_i , and C_i ($i = 1$ to 4) are constants. Functions I_α and K_α are the modified Bessel functions of first and second kind, respectively, where the subscript α denotes the order of the Bessel functions. The boundary conditions [Eqs. (7)–(16)] are linearized as follows:

At $r = 0$,

$$\tilde{v}_r^{(c)} = \frac{\partial \tilde{v}_r^{(c)}}{\partial r} = 0. \quad (32)$$

At the inner interface of the annulus [$r = 1$; Eqs. (9) to (12)],

$$\tilde{v}_r^{(c)} = \Omega \tilde{u}_r^{(e)} \text{ and } \tilde{v}_z^{(c)} = \Omega \tilde{u}_z^{(e)}, \quad (33)$$

$$\tilde{P}_c - \tilde{P}_e - 2 \frac{\partial \tilde{v}_r^{(c)}}{\partial r} + \frac{2}{Y} \frac{\partial \tilde{u}_r^{(e)}}{\partial r} = (K^2 - 1) \varepsilon_i, \quad (34)$$

$$\left(\frac{\partial \tilde{v}_x^{(c)}}{\partial z} + iK \tilde{v}_z^{(c)} \right) - \frac{1}{Y} \left(\frac{\partial \tilde{u}_x^{(e)}}{\partial z} + iK \tilde{u}_z^{(e)} \right) = 0, \quad (35)$$

$$\varepsilon_i = \frac{\tilde{v}_z^{(c)}}{\Omega} \Big|_{r=1}. \quad (36)$$

At the outer interface of the annulus [$r = R_o/R_i = 1/\beta$; Eqs. (13)–(16)],

$$\tilde{P}_e - \tilde{P}_s + \frac{2}{\mu_r} \frac{\partial \tilde{v}_r^{(s)}}{\partial r} - \frac{2}{Y} \frac{\partial \tilde{u}_r^{(e)}}{\partial r} = \frac{1}{\gamma_r} (K^2 - \beta^2) \varepsilon_o, \quad (37)$$

$$\frac{1}{\mu_r} \left(\frac{\partial \tilde{v}_x^{(s)}}{\partial z} + iK \tilde{v}_z^{(s)} \right) - \frac{1}{Y} \left(\frac{\partial \tilde{u}_x^{(e)}}{\partial z} + iK \tilde{u}_z^{(e)} \right) = 0, \quad (38)$$

$$\tilde{v}_r^{(s)} = \Omega \tilde{u}_r^{(e)} \text{ and } \tilde{v}_z^{(s)} = \Omega \tilde{u}_z^{(e)}, \quad (39)$$

$$\varepsilon_o = \tilde{u}_z^{(e)} \Big|_{r=1/\beta} = \frac{\tilde{v}_z^{(s)}}{\Omega} \Big|_{r=1/\beta}. \quad (40)$$

Here, $\gamma_r = \gamma_i/\gamma_o$ is the ratio of the surface tension coefficient at the inner and outer interface of the elastic annulus.

In this study, we consider the viscous fluid surrounding the tube to be unbounded in the r direction. Therefore, the constants C_3 and C_4 can be assumed to be zero because the functions $I_0(Kr)$ and $I_1(Kr)$ go to infinity as $r \rightarrow \infty$. The boundary conditions in Eq. (32) imply that A_2 is zero for the velocity $\tilde{v}_r^{(c)}$ which, at $r = 0$, is finite and zero. Also, A_1 is zero since the flow is assumed to be axisymmetric. Therefore, the general solutions for $\tilde{v}_r^{(c)}$, $\tilde{u}_r^{(e)}$, and $\tilde{v}_r^{(s)}$ [Eqs. (29)–(31)] reduce to the following:

$$\tilde{v}_r^{(c)}(r) = A_3 r I_0(Kr) + A_4 I_1(Kr), \quad (41)$$

$$\tilde{u}_r^{(e)}(r) = B_1 r K_0(Kr) + B_2 K_1(Kr) + B_3 r I_0(Kr) + B_4 I_1(Kr), \quad (42)$$

$$\tilde{v}_r^{(s)}(r) = C_1 r K_0(Kr) + C_2 K_1(Kr). \quad (43)$$

The linearized parameters $\tilde{v}_z^{(c)}$, $\tilde{u}_z^{(e)}$, $\tilde{v}_z^{(s)}$, \tilde{P}_c , \tilde{P}_e , and \tilde{P}_s can be obtained from the above general solutions [Eqs. (41)–(43)]. Substituting these variables ($\tilde{v}_z^{(c)}$, $\tilde{u}_z^{(e)}$, $\tilde{v}_z^{(s)}$, $\tilde{v}_r^{(c)}$, $\tilde{u}_r^{(e)}$, $\tilde{v}_r^{(s)}$, \tilde{P}_c , \tilde{P}_e , and \tilde{P}_s) in the boundary conditions [Eqs. (33)–(35) and (37)–(39)] yields a set of eight homogeneous linear algebraic equations involving eight unknown constants A_i and C_i ($i = 1$ to 2) and B_i ($i = 1$ to 4). Equating the determinant of the coefficient matrix of these linear equations to zero, we obtain the general dispersion relation for the annular cylinder.

The solution of the dispersion relation yields the growth coefficient of the instability as a function of the wave number, $\Omega = f(K, \beta, Y, M, \gamma_r)$. The expression for the general dispersion relation can be written in the form of a determinant of a matrix and is shown in the appendix. The necessary condition for the instability is $\Omega > 0$ for real positive values of K . The dominant growth coefficient (Ω_m) and the corresponding wavelength ($\Lambda_m = 2\pi/K_m$) of instability are obtained by finding the global maxima of Ω and the corresponding wavelength ($\Lambda = 2\pi/K$), respectively, from the dispersion relation.

The modes (squeezing or bending) and the subsequent relative interfacial deformations can also be predicted from the LSA. Prescribing an arbitrary infinitesimal deformation $\tilde{u}_r|_{R_o} = \varepsilon_o$ at the upper elastic-air interface in the r direction, the ratio of the deformations at the inner and outer interfaces of the elastic annulus ($\varepsilon_r = \varepsilon_i/\varepsilon_o$) can be obtained as a function of $g(M, \beta, \gamma_r, Y, K_m, \Omega_m)$. The sign and the magnitude of ε_r yield information about the deformation mode and the resulting relative amplitudes at the interfaces, respectively. The mode of deformation is bending if $\varepsilon_r > 0$ and squeezing ensues

if $\varepsilon_r < 0$. Furthermore, the upper interface deforms more when $|\varepsilon_r| < 1$ and the lower interface deforms more when $|\varepsilon_r| > 1$.

IV. RESULTS AND DISCUSSION

Soft linear elastic cylindrical shells submerged in viscous liquids is a simple biomimetic prototype for the study of the deformations of blood vessels, neurons, and intracellular structures [12,13]. In such systems, the elastic forces and the component of curvature in the axial plane act as stabilizing forces, whereas the radial component of the curvature promotes instability. When the surface tensions at the inner and outer radii of the annulus are the same, the destabilizing capillary pressure at the inner interface is always higher than that at the outer interface of the cylinder and, therefore, the more unstable inner interface would lead to the “pearling” instability of the liquid confined inside the cylinder, as shown in Fig. 2(a). However, when the surface tensions at the inner and outer radii are different, the ratio of the interfacial tensions and the ratio of the inner to outer radii of the cylinder determine the dominant destabilizing force. A more unstable outer interface would lead to the breaking of the elastic cylinder into several toroidal structures or the formation of “sausage-string” [Fig. 2(b)] patterns [18]. Purely kinetic parameters such as the ratio of viscosity of the liquids inside and outside the shell also play a crucial role in the force distribution. A highly viscous fluid associated to one interface always retards its deformation and thus reduces the instability growth rate. Therefore, the radial curvatures of the cylinder at the inner and outer interface can promote instability with different characteristic length scales at the interfaces. For example, a highly viscous fluid at the core can have a stabilizing influence at the inner interface and, thus, the dominant mode can grow by deforming the outer interface more. For such a case, even though the destabilizing force at the inner interface is more, the smaller growth rate at the inner interface makes the upper interface more unstable owing to kinetic reasons.

In what follows, we discuss the results obtained from the linear stability analysis. In particular, we show the effect of the ratios of the inner to outer radius of the elastic cylinder (β), the interfacial tensions at the interfaces, and viscosities of the two fluids on the length and time scales of the instability. We also calculate the relative amplitude and signs of deformations at the two interfaces and predict the dominant mode (bending or squeezing) of instability. In addition, we discuss two asymptotically interesting systems; namely, an elastic fiber submerged in a liquid and a liquid-filled microchannel in an elastic bulk medium. Various asymptotes can be obtained by choosing limiting values of the parameters M and β . The parameter $M = \mu_c/(\mu_c + \mu_s) \rightarrow 0$ can be obtained by substituting either $\mu_c \rightarrow 0$ or $\mu_s \rightarrow \infty$. In the former case, the fluid in the core of the elastic annulus is inviscid. In the latter case, the viscosity of the surrounding fluid tends to infinity and its flow ceases. Another limit of $M = \mu_c/(\mu_c + \mu_s) \rightarrow 1$ can be obtained by setting either $\mu_c \rightarrow \infty$ or $\mu_s \rightarrow 0$. The first case corresponds to a nonflowing rigid core of the elastic tube and the second case denotes an inviscid surrounding fluid. Similarly, $\beta = R_i/R_0 \rightarrow 0$, can be obtained by setting the inner radius to zero, which corresponds to an elastic fiber of radius R_0 . The parameter $\beta \rightarrow 0$ can also be obtained

by choosing $R_0 \rightarrow \infty$ which corresponds to a cylindrical microchannel of radius R_i embedded in an elastic bulk. The physical configurations denoted by these asymptotes should be carefully interpreted from the nondimensional LSA results, which depend on the length scale and time scale chosen for the nondimensionalization. Thus, a proper renormalization of the nondimensional variables becomes necessary for the limiting cases. For example, when μ_c is chosen for the nondimensionalization of the time scale, as done in the equations above, the limiting case of $M \rightarrow 0$ is to be interpreted to mean that μ_c is finite but $\mu_s \rightarrow \infty$. Furthermore, for $M \rightarrow 1$, the nondimensional case corresponds to choosing $\mu_s \rightarrow 0$ rather than the case of $\mu_c \rightarrow \infty$. Similarly, since we have chosen the radius of the inner interface for nondimensionalizing the length scale, the case $\beta \rightarrow 0$ corresponds to $R_0 \rightarrow \infty$ (i.e., a cylindrical channel containing a viscous fluid imbedded in a bulk elastic solid). Thus when we analyze the case of an elastic fiber ($R_i \rightarrow 0$) dipped in a viscous fluid, we would renormalize the length scale with the radius of the outer interface, R_0 , and use μ_s in the nondimensionalization of the time scale.

Soft elastic tubes ($G_e \sim 100$ kPa) become unstable when the inner radius reduces to below a few micrometers. Figure 3(a) shows the variation in the growth rate (Ω) with wave number (K) for two different values of inner radius $R_i = 100$ nm and $R_i = 10$ μ m, respectively, with $\gamma_i = 0.1$ N/m, $G_e = 100$ kPa, $\beta = 0.5$, and $M = 0.5$. For $R_i = 100$ nm ($Y = 10$) the dispersion curve shows positive growth rate implying instability whereas for $R_i = 10$ μ m ($Y = 0.1$) the elastic shell is found to be completely stable. This figure confirms that this type of instability occurs readily for the soft micro- and nanochannels where the effects of the destabilizing radial (cross-sectional) curvatures are stronger than the stabilizing elastic and the in-plane curvatures. Figures 3(b) and 3(c) show the LSA results obtained by varying β when other parameters are held constant at $M = 0.5$, $\gamma_r = 1$, and $Y = 1000$. The parameter $M = 0.5$ and $\gamma_r = 1$ indicate that the viscosity and interfacial tensions at the inner and outer elastic interfaces are equal. Figure 3(b) shows the variation of Ω with K for different values of β . For $\beta = 0.1$, the dominant wave number (K_{\max}) is ~ 0.25 ($\lambda_{\max} = 25.1 R_i$). Figure 3(b) clearly indicates a nonmonotonic change in the dominant wavelength with β as it shows an increase (decrease) in wave number (wavelength) around $\beta = 0.5$. Figure 3(c) shows the variations of the dominant wavelength (Λ_m), dominant growth rate (Ω_m), and the magnitude and sign of the relative deformations at the two interfaces (ε_r) with change in β . For smaller values of β , the elastic tube wall is thick and the destabilizing capillary force at the inner interface is much stronger than at the outer interface. Hence, the instability is governed by the inner interface with the outer surface largely responding to the deformations of the inner surface. Thus, a pearling instability is anticipated under the conditions of a relatively larger deformation at the inner interface [$\varepsilon_r \gg 1$ for low β in Fig. 3(c)]. The positive values of ε_r indicate the bending mode where the interfacial deformations of the two interfaces are in phase with each other. The inset in Fig. 3(c) also shows that Ω_m displays a local minimum with β , after which the deformation of the outer surface becomes more prominent, signaling that a mode changeover from pearling to sausage string occurs. This mode transition is accompanied by an abrupt shift from a

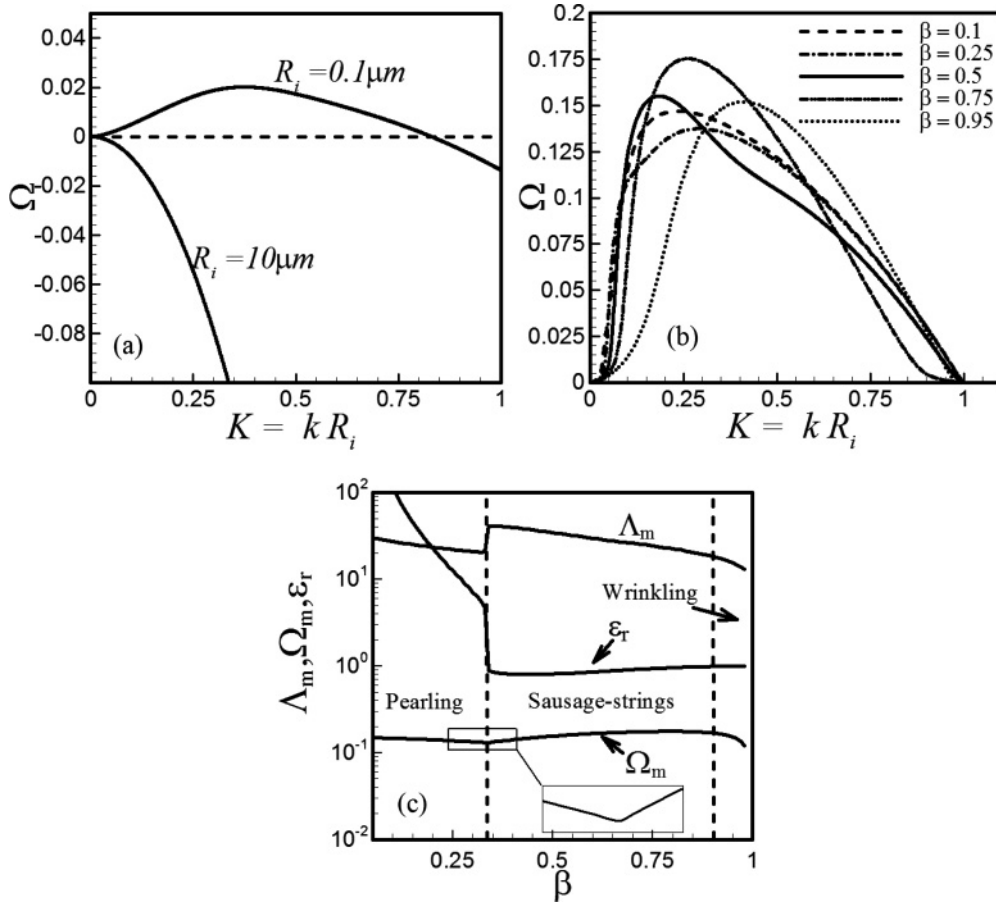


FIG. 3. (a) Dispersion curves for two different values of internal radius of the elastic microtubule. The surface tension coefficient $\gamma_i = 0.1$ N/m and the elastic modulus of the microtubule is assumed to be 100 kPa and parameters $\beta = 0.5$, $\gamma_r = 1$, and $M = 0.5$. The inner radii $R_i = 0.1 \mu\text{m}$ and $10 \mu\text{m}$ correspond to $Y = 10$ and 0.1, respectively. (b) Dispersion curves for different values of β and $Y = 1000$, $\gamma_r = 1$, and $M = 0.5$. (c) Variations in dominant growth rate Ω_m , corresponding wavelength Λ_m , and relative deformation at the inner and the outer interface ϵ_r .

shorter-wave mode (solid line for $\beta = 0.3$ in Fig. 4) to a longer-wave mode (broken line at $\beta = 0.35$) as shown in Fig. 4. Figure 3(c) confirms that the changeover of modes takes place at $\beta_c \sim 0.33$ and the bimodal behavior of the Ω vs K plots [Fig. 3(b)] confirms the coexistence of both pearling and sausage-string modes in the transition region near β_c . The changeover of the dominant mode from the inner to outer interface is reflected in the sharp change of ϵ_r from ~ 5 to ~ 0.86 in Fig. 3(c), which suggests that, for $\beta < \beta_c$, the inner interface deforms more, resulting in the pearling instability, whereas, for $\beta > \beta_c$, the outer interface deforms more, leading to the sausage-string instability. Figure 3(c) also shows that the instability now grows by adopting an in-phase “bending” mode ($\epsilon_r > 0$) with larger deformation at the outer interface ($\epsilon_r < 1$).

The transition from pearling to sausage-string instabilities can be envisaged in the following manner: (a) The pearling instability with a shorter wavelength is observed for the destabilizing force because the inner radial curvature is dominant at low β . (b) Upon increasing β , as the thickness of the elastic tube reduces, a transition zone appears where the inner wall deforms more to promote a pearling but the outer wall deforms enough to cause a sausage-string instability

to the elastic tube. In this situation, although the outer wall deforms less under a weaker destabilizing radial curvature force corresponding to the outer interface, it still deforms enough to cause the sausage-string instability to the thinner elastic tube near $\beta \sim \beta_c$. (c) For thinner elastic shells ($\beta > \beta_c$), the sausage-string instability dominates over the pearling instability mode. Since the sausage-string instability is governed by the weaker destabilizing radial curvature force, corresponding to the outer interface, it grows with a larger wavelength as compared with the pearling instability. Figure 3(c) shows that, near the transition zone and after the upward jump in Λ_m , it again continues to decrease because, with increasing β , the strength of the destabilizing radial curvature corresponding to the outer interface increases. Interestingly, when β is further increased, the inner-surface amplitude increases more than the outer one, which shows saturation. At a high value of $\beta \sim 0.95$, both amplitudes grow to a similar magnitude of $\epsilon_r \approx 1.0$, which corresponds to a pure bending mode without a change in the tube thickness. This is referred to as the “wrinkling” instability of the elastic tube. The wrinkling instabilities occur when the elastic shell is very thin and noncompliant [47]. The compliance of the shell can nominally be defined as the ratio of the thickness of the shell to the shear modulus of the tube.

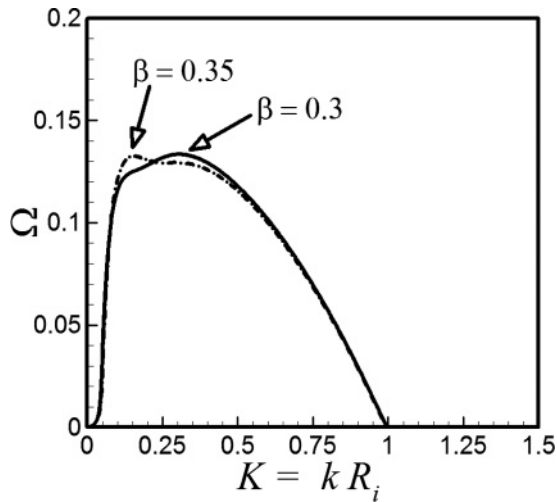


FIG. 4. Dispersion curves for $\beta = 0.3$ and 0.35 showing jump in the most dominant wavelength.

The reduction in Ω_m and Λ_m at high values of β (>0.9) can also be attributed to the lesser compliance for thinner shells. Figures 3 and 4 clearly show that, with the variation in β , three distinct domains (i.e., pearling, sausage-string, and wrinkling instabilities) can be obtained for an elastic shell surrounded by viscous liquids.

Figure 5 demonstrates that the kinetic parameters such as viscosity can strongly influence the onset of the instability and transition to different modes. Fig. 5(a) shows variations in Ω_m , Λ_m , and ε_r with M for $\beta = 0.5$, $\gamma_r = 1$, and $Y = 1000$. For lower values of M , when the liquid in the core is less viscous, the most dominant wavelength is shorter and a pearling mode is observed at the inner interface. With an increase in M , a jump is observed in Λ_m to a higher value at $M_c = 0.28$. The ε_r plot in this figure confirms that, for $M < M_c$, a pearling instability mode ($\varepsilon_r > 1$) persists whereas the sausage-string mode ($\varepsilon_r < 1$) appears for $M > M_c$. Figure 5(b) shows the bimodal behavior of the Ω vs K plots near M_c , which clearly shows the jump in the dominant mode from the shorter wavelengths for low values of M [solid line for $M = 0.25$ in Fig 5(b)] to

longer wavelengths for $M > M_c$ (broken line for $M = 0.30$). A comparison between Figs. 3(c) and 5(a) reveals that that, when the viscosities of the liquid in the core and surrounding are same ($M = 0.5$), the transition from pearling to sausage-string mode occurs at a lower $\beta = 0.33$ [Fig. 3(c)]. When the inner core has lower viscosity [$M = 0.28$; Fig. 5(a)], the changeover of modes takes place at a higher $\beta = 0.5$. A lowering of the inner viscosity allows the inner interface to be more unstable, so that the transition to sausage strings can occur only when the destabilization engendered by the outer cross-sectional curvature is made stronger by a further decrease in the outer radius. Thus, the kinetic parameters such as the ratio of the viscosity of the fluids in the core and the surrounding medium can substantially influence the condition for transition from pearling and sausage-string instabilities or vice versa. Beyond $M > M_c$, a progressive reduction of Λ_m is observed whereas, in the absence of any viscous resistance in the surrounding medium, Ω_m sharply increases as $M \rightarrow 1$. Interestingly, the plot of ε_r in Fig. 5(a) indicates that, for $M \rightarrow 0$, when the viscous resistance at the outer elastic wall is much higher compared to the inner wall, the instability is dominated by the deformation of the inner interface ($\varepsilon_r \gg 1$). However, when $M \rightarrow 1$ ($\mu_s \rightarrow 0$) the lower viscous resistance felt at the outer surface allows it to govern the amplitude ($\varepsilon_r \ll 1$) and the length scale of the instability. These asymptotes provide us with two different systems, of which the former corresponds to an elastic shell with a viscous core and surrounded by a highly viscous nonflowing liquid (like a rigid hollow cylinder) and the latter corresponds to an elastic shell with a highly viscous nonflowing liquid (a rigid fiber) in the core. The dominant mode of instability in the former has a wavelength $\sim 15R_i$ whereas the latter shows patterns with wavelength $\sim 21R_i$.

The other parameters that can significantly influence the transition of the instability modes are the ratio of the interfacial tensions at the interfaces (γ_r) and the ratio of the surface tension to the elastic force (Y). Figure 6(a) shows the variations in Λ_m , Ω_m , and ε_r with γ_r for $\beta = 0.5$, $M = 0.5$, and $Y = 1000$. For $\gamma_r < 2$, the value of $\varepsilon_r < 1$ suggests that the outer interface deforms more than the inner surface of the elastic annulus.

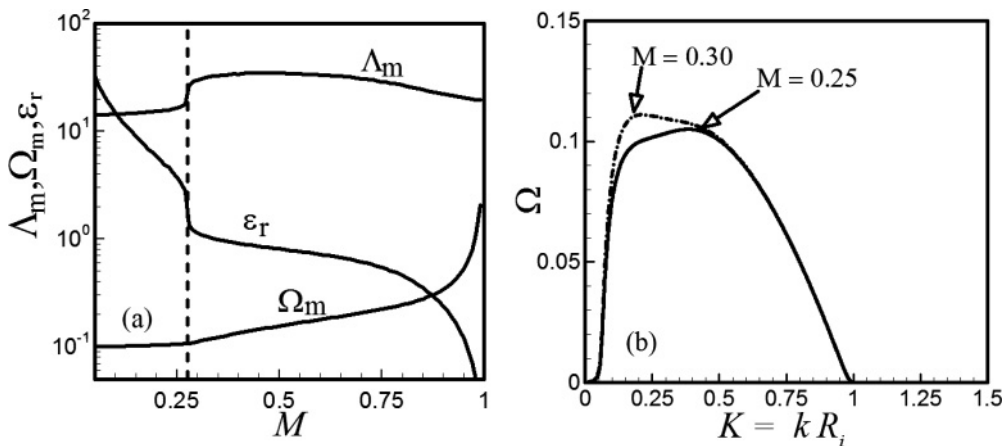


FIG. 5. (a) Variation in most dominant wavelength Λ_m , corresponding growth rate Ω_m , and relative deformation at the inner and the outer interface ε_r , with M and $Y = 1000$, $\gamma_r = 1$, and $\beta = 0.5$. (b) Dispersion curves for $M = 0.25$ and 0.3 showing jump in the most dominant wavelength. The critical β for $M = 0.33$ is 0.5 .

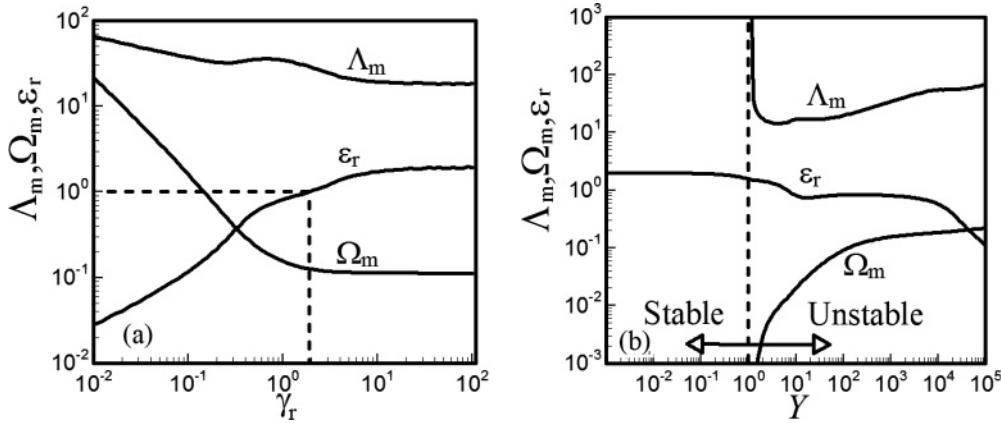


FIG. 6. Variation in most dominant wavelength Λ_m , corresponding growth rate Ω_m , and relative deformation at the inner and the outer interface ϵ_r (a) with γ_r and $Y = 1000$, $M = 0.5$, and $\beta = 0.5$ and (b) with Y and $\gamma_r = 1$, $M = 0.5$, and $\beta = 0.5$.

For very small values of γ_r , the capillary force at the outer interface is much stronger than the one at the inner interface and therefore the sausage-string mode dominates. The figure also shows that Ω_m and Λ_m monotonically decrease with an increase in γ_r and become nearly constant beyond $\gamma_r > 2$, where a pearling instability is expected because $\epsilon_r > 1$. For higher values of γ_r , the wavelength corresponds to the destabilizing capillary force at the inner interface. Figure 6(b) shows variations in Λ_m , Ω_m , and ϵ_r with Y . Other parameters are held constant at the following values: $\gamma_r = 1$, $M = 0.5$, and $\beta = 0.5$. The value of Λ_m first decreases and then monotonically increases with an increase in Y . The elastic annulus is stable below a critical value of $Y_c \sim 1$. With an increase in Y beyond Y_c , ϵ_r decreases and goes below 1, suggesting that, for higher values of Y (i.e., for softer annuli), the outer interface deforms more. Figure 7 shows variation in the critical value of Y_c with β . For $\beta \rightarrow 0$, Y_c asymptotically tends to 2. The case $\beta \rightarrow 0$ represents the asymptote of a microchannel in a bulk elastic medium. With an increase in β , Y_c decreases and tends to zero for $\beta \rightarrow 1$. The asymptote $\beta \rightarrow 1$ represents the case where there is no elastic medium

between the two fluids (core and surrounding) and therefore no resistance to instability at the fluid-fluid interface.

The general analysis presented here can also be asymptotically reduced to analyze a micro- or nanochannel in a semi-infinite elastic solid. For such a case, the deformation field in the elastic medium is bounded at $r \rightarrow \infty$ and therefore the coefficients B_3 and B_4 are identically zero in the analysis described in Sec. II. Thus, a reduced dispersion relation for the spontaneous deformation of a microchannel in an elastic bulk is obtained. Figure 8 shows the dominant wave number and the corresponding growth coefficient for different values of Y . Figure 8 clearly shows that the critical value beyond which the instability occurs is $Y_c = 2$, which was also obtained as an asymptotic case from the analysis of an elastic tube ($\beta \rightarrow 0$ in Fig. 7). For larger values of Y , elastic forces are weaker, which leads to longer wavelengths as the shorter wavelengths are stabilized by the in-plane capillary force. As expected, the growth coefficient increases with an increase in Y because the destabilizing capillary force is enhanced.

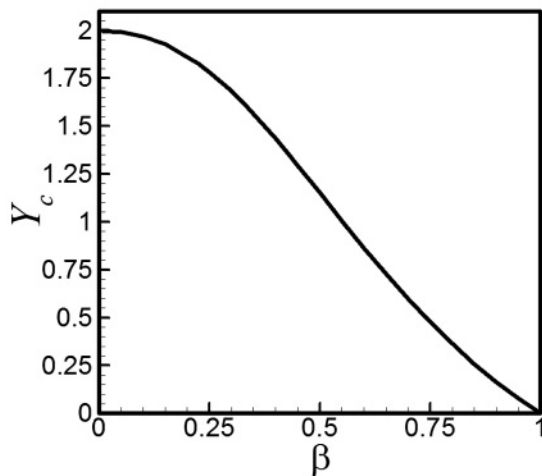


FIG. 7. Variation in Y_c with β . Other parameters are held constant at $\gamma_r = 1$ and $M = 0.5$.

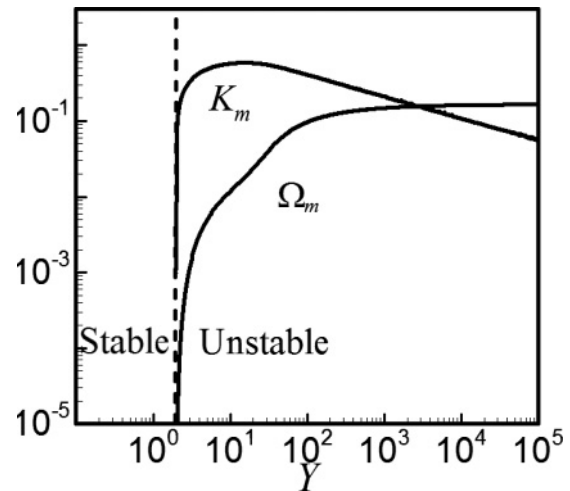


FIG. 8. Variation in K_m and Ω_m with Y for a cylindrical microchannel cut into an elastic medium. The dashed line marks the critical Y below which the microchannel would be stable to the Rayleigh instability.

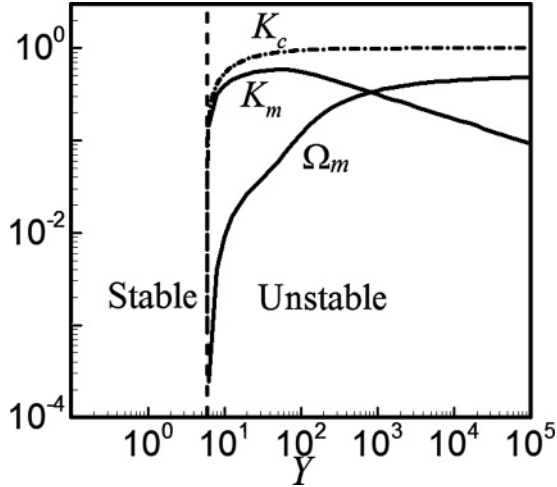


FIG. 9. Variation in K_m and Ω_m with Y for a soft elastic fiber. The dashed line shows the critical Y below which the microfiber is stable to the Rayleigh instability.

Another asymptotic system that can easily be analyzed from the general formulation shown in Sec. II is the deformation of an elastic fiber submerged in a bulk viscous fluid. The renormalized dispersion relation is now obtained by setting the coefficients B_1 and B_2 to zero because the terms multiplying these diverge as $r \rightarrow 0$. The scaling parameters used here to study this case of a solid fiber are $K = kR_o$, $\Omega = \omega\mu_s R_o/\gamma_o$ and $Y = \gamma_o/(G_e R_o)$. Note that the radius and surface tension of the outer surface of the annular cylinder, R_o , and the viscosity of the surrounding medium has been used for nondimensionalization. Figure 9 shows the dominant wave number and the corresponding growth rate as a function of Y . Interestingly, the trend is similar to that discussed earlier for a micro- or nanochannel. However, the critical value of Y below which the fiber is stable is 6 as compared to 2 for a microchannel in an elastic medium. The critical value of Y is higher for an elastic fiber because it is less compliant compared to the elastic bulk containing the microchannel. Interestingly, the critical value of $Y_c = 6$ for the onset of instability in elastic fibers ($Y_c = 2$ for a microchannel) is independent of the surrounding (core) viscous fluid. Figure 9 also shows that the critical wave number for an elastic fiber increases with an increase in Y and asymptotically attains a value which can be predicted purely based on the minimization of the free energy, neglecting the elastic energy penalty ($k_c R_o = 1$). This is not surprising because, in the limit of zero shear modulus, the elastic fibers would behave like an inviscid fluid and deform without any resistance. This also validates our linear stability analysis results.

V. CONCLUSIONS

We performed a linear stability analysis (LSA) on an initially quiescent system to show that, below a critical shear modulus [$Y = \gamma_i/(G_e R_i) > 1$ for $\gamma_r = 1$, $M = 0.5$, and $\beta = 0.5$], an elastic annulus is unstable and may show one of the following modes of instability: (i) a pearling instability where the inner interface deforms more than the outer interface, (ii) sausage strings with the formation of beads when the outer

interface deforms more and may even lead to the breakup of the annulus into rings, and (iii) wrinkling when the wall of the annulus is thin and both inner and outer interfaces deform equally (see Fig. 2). Instability is the result of a competition between the elastic penalty due to deformation in the tube and the destabilizing radial curvature at the inner and the outer interfaces. Both the inner interface of the annulus and the outer interface have different characteristic lengths, and kinetic effects choose the dominant mode.

Based on the results from linear stability analysis, we show that a thicker elastic tube would show breakup of the inner fluid cylinder into a string of pearls or a peapod, whereas an extremely thinner elastic tube shows bending modes (wrinkling) with shorter wavelengths. In the intermediate regime one would observe the formation of sausage strings with the outer surface deforming more than the inner interface. Such instabilities have been observed in the breakup of polymer nanotubes into capsules and in blood vesicles, which show the formation of sausage strings [18].

We also show that a thin microchannel in an elastic bulk can be stable and rupture into thin spherical cavities if the parameter Y is greater than 2. A thin soft elastic fiber would break up into droplets like a liquid jet if the parameter Y is greater than 6. With the advent of nanomanufacturing and the miniaturization of existing systems to enhance efficiency and reduce power consumption, the present study provides guidelines for designing stable microfibers, microtubes, and microvessels.

ACKNOWLEDGMENTS

Discussions with V. Shankar, IITK, are gratefully acknowledged. The support of Ministry of Education, Science and Technology, South Korea under the World Class University (WCU) is acknowledged by Ashutosh Sharma under program R32-2008-000-20082-0.

APPENDIX

The dispersion relation can be written in the determinant form:

$$\begin{vmatrix} a_{11} & a_{12} & \cdots & a_{17} & a_{18} \\ a_{21} & & & & a_{28} \\ \vdots & & \ddots & & \vdots \\ a_{71} & & & & a_{78} \\ a_{81} & a_{82} & \cdots & a_{87} & a_{88} \end{vmatrix} = 0.$$

The nonzero components of the matrix are given in terms of the modified Bessel functions of the first and second kind:

$$\begin{aligned} a_{13} &= [\Omega K_0(K/\beta)]/\beta, & a_{14} &= \Omega K_1(K/\beta), \\ a_{15} &= [\Omega I_0(K/\beta)]/\beta, & a_{16} &= \Omega I_1(K/\beta), \\ a_{17} &= -[K_0(K/\beta)]/\beta, & a_{18} &= -K_1(K/\beta), \end{aligned}$$

$$\begin{aligned} a_{21} &= -I_0(K), & a_{22} &= -I_1(K), & a_{23} &= \Omega K_0(K), \\ a_{24} &= \Omega K_1(K), & a_{25} &= \Omega I_0(K), & a_{26} &= \Omega I_1(K), \end{aligned}$$

$$\begin{aligned}
a_{33} &= \frac{\Omega[2\beta K_0(K/\beta) - K K_1(K/\beta)]}{\beta^2}, & a_{54} &= \frac{2K^2 K_1(K/\beta)}{Y}, & a_{55} &= \frac{2K[K I_0(K/\beta) + \beta I_1(K/\beta)]}{Y\beta}, \\
a_{34} &= -\frac{K\Omega K_0(K/\beta)}{\beta}, & a_{35} &= \frac{\Omega[2\beta I_0(K/\beta) + K I_1(K/\beta)]}{\beta^2}, & a_{56} &= \frac{2K^2 I_1(K/\beta)}{Y}, \\
a_{36} &= \frac{K\Omega I_0(K/\beta)}{\beta}, & a_{37} &= \frac{-2\beta I_0(K/\beta) + K I_1(K/\beta)}{\beta^2}, & a_{57} &= \frac{2K(M-1)[K K_0(K/\beta) - \beta K_1(K/\beta)]}{M\beta}, \\
a_{38} &= \frac{K K_0(K/\beta)}{\beta}, & a_{58} &= \frac{2K^2(M-1)K_1(K/\beta)}{M}, \\
a_{41} &= -2I_0(K) - K I_1(K), & a_{42} &= -K I_0(K), & a_{61} &= -2K[K I_0(K) + I_1(K)], & a_{62} &= -2K^2 I_1(K), \\
a_{43} &= \Omega[2K_0(K) - K K_1(K)], & a_{63} &= \frac{2K[K K_0(K) - K_1(K)]}{Y}, \\
a_{44} &= -K\Omega K_0(K), & a_{45} &= \Omega[2I_0(K) + K I_1(K)], & a_{64} &= \frac{2K^2 K_1(K)}{Y}, & a_{65} &= \frac{2K[K I_0(K) + I_1(K)]}{Y}, \\
a_{46} &= K\Omega I_0(K), & a_{66} &= \frac{2K^2 I_1(K)}{Y}, \\
a_{53} &= \frac{2K[K K_0(K/\beta) - \beta K_1(K/\beta)]}{Y\beta},
\end{aligned}$$

$$\begin{aligned}
a_{73} &= \frac{2K K_1(K/\beta)}{Y\beta}, & a_{74} &= \frac{2[K K_0(K/\beta) + \beta K_1(K/\beta)]}{Y}, & a_{75} &= -\frac{2K I_1(K/\beta)}{Y\beta}, \\
a_{76} &= \frac{2[-K I_0(K/\beta) + \beta I_1(K/\beta)]}{Y}, & a_{77} &= \frac{M(\beta^2 - K^2)K_0(K/\beta) + 2K(M-1)\gamma_r\Omega K_1(K/\beta)}{M\beta\gamma_r\Omega}, \\
a_{78} &= \frac{2K(M-1)\gamma_r\Omega K_0(0, K/\beta) + [-K^2M + \beta(M\beta - 2\gamma_r\Omega + 2M\gamma_r\Omega)]K_1(1, K/\beta)}{M\gamma_r\Omega}, \\
a_{81} &= -\frac{(K^2 - 1)I_0(K) + 2K\Omega I_1(K)}{\Omega}, & a_{82} &= \frac{-2K\Omega I_0(K) + (1 - K^2 + 2\Omega)I_1(K)}{\Omega}, & a_{83} &= -\frac{2K K_1(K)}{Y}, \\
a_{84} &= -\frac{2[K K_0(K) + K_1(K)]}{Y}, & a_{85} &= \frac{2K I_1(K)}{Y}, & a_{86} &= \frac{2[K I_0(K) - I_1(K)]}{Y}.
\end{aligned}$$

- [1] M. W. J. Prins, W. J. J. Welters, and J. W. Weekamp, *Science* **291**, 277 (2001).
- [2] M. A. Unger, H. Chou, T. Thorsen, A. Scherer, and S. R. Quake, *Science* **288**, 113 (2000).
- [3] G. M. Whitesides and A. D. Stroock, *Phys. Today* **54**, 42 (2001).
- [4] D. V. McAllister, M. G. Allen, and M. R. Prausnitz, *Annual Review of Biomedical Engineering* **2**, 289 (2000).
- [5] M. R. Abidian, D. H. Kim, and D. C. Martin, *Advanced Materials* **18**, 405 (2006).
- [6] A. Migliore, F. Vozi, G. Vozi, and A. Ahluwalia, *Biomed Microdevices* **10**, 81 (2008).
- [7] R. Dersch, M. Steinhart, U. Boudriot, A. Greiner, and J. H. Wendorff, *Polym. Adv. Technol.* **16**, 276 (2005).
- [8] J. Jang, S. Ko, and Y. Kim, *Adv. Funct. Mater.* **16**, 754 (2006).
- [9] K. Sekimoto and K. Kawasaki, *J. Phys. Soc. Jpn.* **56**, 2997 (1987).
- [10] A. Onuki, *Phys. Rev. A* **39**, 5932 (1989).
- [11] E. S. Matsuo and T. Tanaka, *J. Chem. Phys.* **89**, 1695 (1988).
- [12] E. S. Matsuo and T. Tanaka, *Nature (London)* **358**, 482 (1992).
- [13] P. Nelson, T. Powers, and U. Seifert, *Phys. Rev. Lett.* **74**, 3384 (1995).
- [14] B. Barriere, K. Sekimoto, and L. Leibler, *J. Chem. Phys.* **105**, 1735 (1996).
- [15] D. E. Discher and A. Eisenberg, *Science* **297**, 967 (2002).
- [16] Q. He, W. Song, H. Möhwald, and J. Li, *Langmuir* **24**, 5508 (2008).
- [17] I. Tsafirir, Y. Caspi, M. Guedeau-Boudeville, T. Arzi, and J. Stavans, *Phys. Rev. Lett.* **91**, 138102 (2003).
- [18] P. Alström, V. M. Eguíluz, M. Colding-Jørgensen, F. Gustafsson, and N. Holstein-Rathlou, *Phys. Rev. Lett.* **82**, 1995 (1999).
- [19] J. Xie, X. Li, and Y. Xia, *Macromol Rapid Commun.* **29**, 1775 (2008).
- [20] D. H. Reneker and I. Chun, *Nanotechnology* **7**, 216 (1996).
- [21] K. Autumn, Y. A. Liang, S. T. Hsieh, W. Zesch, W. P. Chan, T. W. Kenny, R. Fearing, and R. J. Full, *Nature (London)* **405**, 681 (2000).
- [22] T. S. Kustandi, V. D. Samper, D. K. Yi, W. S. Ng, P. Neuzil, and W. Sun, *Adv. Funct. Mater.* **17**, 2211 (2007).

- [23] N. J. Glassmaker, A. Jagota, C.-Y. Hui, and J. Kim, *J. R. Soc. Interface* **1**, 23 (2004).
- [24] M. T. Northen, C. Greiner, E. Arzt, and K. L. Turner, *Adv. Mater.* **20**, 3905 (2008).
- [25] D. Chandra and S. Yang, *Langmuir* **25**, 10430 (2009).
- [26] J. W. Strutt and Lord Rayleigh, *Philosophical Magazine Ser. 5* **34**, 177 (1892).
- [27] J. Plateau, *Acad. Sci. Bruxelles Mém.* **23**, 5 (1849).
- [28] Lord Rayleigh, *Proc. Roy. Soc. Lond.* **29**, 71 (1879).
- [29] J. Eggers and E. Villermaux, *Rep. Prog. Phys.* **71**, 036601 (2008).
- [30] M. S. McCallum, P. W. Voorhees, M. J. Miksis, S. H. Davis, and H. Wong, *J. Appl. Phys.* **79**, 7604 (1996).
- [31] F. Yang and W. Song, *Int. J. Solid Struct.* **43**, 6767 (2006).
- [32] A. Ghatak, M. Chaudhury, V. Shenoy, and A. Sharma, *Phys. Rev. Lett.* **85**, 4329 (2000).
- [33] V. Shenoy and A. Sharma, *Phys. Rev. Lett.* **86**, 119 (2001).
- [34] W. Monch and S. Herminghaus, *Europhys. Lett.* **53**, 525 (2001).
- [35] V. Shenoy and A. Sharma, *J. Mech. and Phys. Solids* **50**, 1155 (2002).
- [36] C. Q. Ru, *J. Appl. Mech.* **69**, 97 (2002).
- [37] H. Hsueh and P. Miranda, *J. Mater. Res.* **18**, 1275 (2003).
- [38] R. E. Webber and K. R. Shull, *Phys. Rev. E* **68**, 021805 (2003).
- [39] S. Kumar, *Langmuir* **19**, 2473 (2003).
- [40] S. Kumar and O. K. Matar, *J. Colloid Interface Sci.* **273**, 581 (2004).
- [41] J. Sarkar, V. Shenoy, and A. Sharma, *Phys. Rev. Lett.* **93**, 018302 (2004).
- [42] G. F. Wang, P. Schiavone, and C. Q. Ru, *Acta Mechanica* **180**, 1 (2005).
- [43] O. K. Matar, V. Gkanis, and S. Kumar, *J. Colloid Interface Sci.* **286**, 319 (2005).
- [44] S.-Q. Huang, Q.-Y. Li, X.-Q. Feng, and S.-W. Yu, *Mechanics Of Materials* **38**, 88 (2006).
- [45] S. J. Kwon, *J. App. Phys.* **99**, 063503 (2006).
- [46] S. J. Kwon and J. G. Park, *J. Phys. Chem. C* **111**, 4404 (2007).
- [47] C. D. Coman and A. P. Bassom, *J. Mech. Phys. Solids* **55**, 1601 (2007).
- [48] H. Zeng, Y. Tian, B. Zhao, M. Tirrell, and J. Israelachvili, *Macromolecules* **40**, 8409 (2007).
- [49] J. Sarkar, V. Shenoy, and A. Sharma, *Phys. Rev. E* **77**, 031604 (2008).
- [50] C. C. Lin, F. Q. Yang, and S. Lee, *Langmuir* **24**, 13627 (2008).
- [51] J. Nase, A. Lindner, and C. Creton, *Phys. Rev. Lett.* **101**, 074503 (2008).
- [52] D. Bandyopadhyay, A. Sharma, and V. Shankar, *J. Chem. Phys.* **128**, 154909 (2008).
- [53] D. Bandyopadhyay, A. Sharma, U. Thiele, and P. D. S. Reddy, *Langmuir* **25**, 9108 (2009).
- [54] X.-H. Pan, S.-Q. Huang, S.-W. Yu, and X.-Q. Feng, *J. of Phys. D-App. Phys.* **42**, 055302 (2009).
- [55] L. H. He and K. Li, *Thin Solid Films* **518**, 3853 (2010).
- [56] C. W. Lim and X. S. Xu, *App. Mech. Rev.* **63**, 050802 (2010).
- [57] D. Bandyopadhyay, A. Sharma, and V. Shankar, *Euro. Phys. Lett.* **89**, 36002 (2010).
- [58] B. Li, H. P. Zhao, and X. Q. Feng, *J. Mech. and Phys. Solids* **59**, 610 (2011).
- [59] N. Arun, A. Sharma, V. Shenoy, and K. S. Narayan, *Adv. Materials* **18**, 660 (2006).
- [60] J.-Y. Chung, K. Kim, M. K. Chaudhury, J. Sarkar, and A. Sharma, *Euro. Phys. J. E* **20**, 47 (2006).
- [61] M. Gonuguntala, A. Sharma, J. Sarkar, S. A. Subramanian, M. Ghosh, and V. Shenoy, *Phys. Rev. Lett.* **97**, 018303 (2006).
- [62] M. Gonuguntala, A. Sharma, R. Mukherjee, and S. A. Subramanian, *Langmuir* **22**, 7066 (2006).
- [63] R. Mukherjee, R. Pangule, A. Sharma, and G. Tomar, *Adv. Func. Mat.* **17**, 2356 (2007).
- [64] N. Arun, A. Sharma, P. S. G. Pattader, I. Banerjee, H. M. Dixit, and K. S. Narayan, *Phys. Rev. Lett.* **102**, 254502 (2009).